High-temperature oxidation and reduction of the inverse ceria/Cu(111) catalyst characterized by LEED, STM, nc-AFM and KPFM

Ali El Barraj, Baptiste Chatelain, Clemens Barth

High-temperature oxidation and reduction of the inverse ceria/Cu(111) catalyst characterized by LEED, STM, nc-AFM and KPFM

Ali El Barraj, Baptiste Chatelain and Clemens Barth

Aix-Marseille Univ, CNRS, CINaM, Marseille, France

E-mail: barth@cinam.univ-mrs.fr

Abstract. The inverse catalyst 'cerium oxide (ceria) on copper' has attracted much interest in recent time because of its promising catalytic activity in the water-gas-shift reaction and the hydrogenation of CO_2. For such reactions it is important to study the redox behaviour of this system, in particular with respect to the reduction by H_2. Here, we investigate the high-temperature O_2 oxidation and H_2 reduction of ceria nanoparticles (NP) and a Cu(111) support by low energy electron diffraction (LEED), scanning tunnelling microscopy (STM), non-contact atomic force microscopy (nc-AFM) and Kelvin probe force microscopy (KPFM). After oxidation at 550 °C, the ceria NPs and the Cu(111) support are fully oxidized, with the copper oxide exhibiting a new oxide structure as verified by LEED and STM. We show that a high H_2 dosage in the kilo Langmuir range is needed to entirely reduce the copper support at 550 °C. A work function (WF) difference of $\triangle\phi_{\mathrm{rCeria/Cu\text{-}Cu}} \approx$ -0.6 eV between the ceria NPs and the metallic Cu(111) support is measured, with the Cu(111) surface showing no signatures of separated and confined surface regions composed by a CuCe alloy. After oxidation, the WF difference is close to zero ($\triangle\phi_{\mathrm{Ceria/Cu\text{-}Cu}} \approx$ -0.1 . . . 0 eV), which probably is due to a WF change of both, ceria and copper.

Keywords: Cerium oxide (ceria), Cu(111), oxidation, reduction, work function, low energy electron diffraction (LEED), scanning probe microscopy (SPM)

Submitted to: *J. Phys.: Condens. Matter*

1. Introduction

Cerium oxide (ceria) is an important reducible oxide in heterogeneous catalysis [1, 2] due to its high oxygen storage capacity (OSC), which is based on the oxidation and reduction of cerium atoms and the accompanied filling and creation of oxygen vacancies, respectively [3]. Apart from other applications, ceria is used in the water-gas-shift reaction [4, 5], the oxidation of hydrocarbons [5, 1] and in fuel cells [6, 7, 8], with the most prominent application being the three-way-catalyst [9, 2]. Insights into ceria's morphology, atomic structure and surface chemistry are obtained by surface science studies, which are mostly conducted under UHV conditions. In particular, model surfaces in the form of thick [10] and ultra-thin films [11, 12, 13, 14] have been studied in the recent past with standard surface science techniques.

Many studies deal with the conventional metal/ceria catalyst where ceria plays the role as a support for metal nanoparticles (NP) (e.g., PdNPs [15, 16], AuNPs [17], AgNPs [18]). However, the inverse catalyst composed of a metal surface supporting ceria (ceria/metal catalyst) can be more catalytically active [14]: for instance, the methanol production trough the hydrogenation of CO_2 is higher on ceria/Cu compared to Cu/ceria [19, 20], which is also the case in the water-gas-shift (WGS) reaction [21].

When dealing with the inverse catalyst, the redox behaviour of ceria but also of the metal support has to be considered. For instance, metal surfaces like Pt(111) can form locally an alloy with cerium upon reduction [22]. The alloy then serves as a cerium reservoir that is used to form new ceria upon oxidation [23]. A similar mechanism can be observed on gold surfaces [24], where not an alloy but small NPs of cerium are formed from the released cerium [25]. Apart from forming an alloy, the metal surface can also form a surface oxide upon oxidation, as it is the case for ceria on Cu(111) [21]. When reducing the latter system by, e.g., CO, the copper oxide transforms back into its metallic state [26]. From these perspectives it is evident that the metal modifies the reaction conditions during a redox cycle in dependence on its different states.

To study the role of a metal support that changes its state between being metallic and oxidized, the inverse ceria/Cu(111) catalyst is an ideal model surface [21, 26]. The ceria/Cu(111) system has been extensively studied in the past [27], particularly by LEED [28, 29, 30, 31, 32, 33, 34, 35, 36, 37], RHEED [38, 15], LEEM [39, 40, 41], XPS [29, 30, 42, 26, 43, 44, 33, 34, 45, 35, 20, 46, 36, 47, 37, 15, 48, 41] and by STM [30, 32, 26, 49, 33, 34, 45, 35, 46, 36, 47, 37] as well as by density functional theory (DFT) [21, 26, 49, 50, 19, 51, 41]. Apart from the morphology, atomic structure and oxidation state of ceria, the reduction of ceria by CO [30, 26], H_2[19, 41], atomic H [44], Ce [33, 34, 37] and the interaction with CO_2 [47], H_2O [44] and SO_2 [43] were studied as well as some reactions like the water-gas-shift reaction [21], CO oxidation [26] and the hydrogenation of CO_2 at high H_2 and CO_2 partial pressures [19, 20].

Whereas many studies deal with ceria films that almost entirely cover Cu(111), it is only a few that consider the inverse catalyst, mentioning either briefly copper oxide [19, 35, 41] or focusing in some detail on the oxidation of the copper substrate in the presence of ceria [26]. With respect to the reduction by H_2, two studies can be found in which very long H_2 exposures of one day were applied, either with a very high H_2 pressure in the mbar range and with the sample kept at room temperature [19] or with a pressure in the 10^{-6} mbar range and a sample temperature of 427 °C [41].

In this work we investigate the high-temperature redox behaviour at 550 °C of the inverse catalyst ceria/Cu(111), which is composed of nanometre high ceria nanoparticles (NP) on Cu(111). Oxidation and reduction experiments are done with O_2 and H_2, respectively, both being in the 10^{-6} mbar range. We show that the system can be put either into its fully oxidized (O_2 oxidation) or a mixed state (H_2 reduction), with copper entirely reduced and ceria being close to CeO_2 stoichiometry. We report on a new copper oxide structure that is formed after the oxidation and comment on the work function (WF) difference between supported ceria and the copper support, which depends on the oxidation state of the system.

2. Methods

A detailed description of the sample preparation and material properties (absolute WF value for Cu(111), lattice constants of Cu and CeO_2) as well as descriptions of our LEED, STM, nc-AFM and KPFM can be found in the supplementary information. Here, we summarize the most important details.

2.1. Synthesis of ceria NPs

The Cu(111) substrate is cleaned by repeated cycles of sputtering at 1.5 keV and following UHV annealing at 550 °C. Ceria NPs are grown by evaporation of Ce within 10 minutes onto the Cu(111) surface, which is kept at room temperature (RT). After the Ce deposition, the crystal is heated up in an UHV oven from RT to 550 °C in 3×10^{-6} mbar O_2 within 15 to 20 minutes. Afterwards, the sample remains for 10 minutes at 550 °C in O_2 and is then cooled down to 300 °C within 15 minutes and still in O_2. The cooling in O_2 avoids a possible reduction of the ceria film as mentioned before for ceria/Pt(111) films [52]. At 300 °C, the sample is extracted from the oven and the O_2 supply is stopped. The nominal thickness of the grown ceria is around (5.7 ± 0.5) mono-layers (ML).

2.2. Oxidation/reduction experiments

The sample is placed into the UHV oven at 300 °C and the temperature is increased such that it reaches $T_{\max} = 550$ °C. After the annealing at $T_{\max}$, the temperature is decreased onto 300 °C and the crystal is extracted from the oven. When annealing the sample only under UHV conditions, the pressure remains in the lower 10^{-10} mbar pressure region. In the case of O_2, the O_2 exposure is started at $T_{\max}$ and is not stopped during the cooling until a temperature of 300 °C is reached, due to the reasons mentioned above. The same is done during H_2 annealing if not otherwise specified (see Table 1 and below).

2.3. SPM and LEED

STM, frequency modulated nc-AFM and KPFM experiments as well as LEED experiments are performed in the same UHV chamber (1×10^{-10} mbar base pressure) [53] at room temperature. KPFM is used in the frequency modulation mode [54] and applied during the nc-AFM imaging in the constant $\triangle f$ mode. During the scanning of the surface, the electrostatic tip-surface interaction is minimized at each image point by the bias voltage, yielding the contact potential difference (CPD) between tip and

Table 1. All redox steps conducted with the ceria/Cu(111) sample in dependence on the redox cycle number (No.). A redox annealing step is done at $T_{\max} = 550\,^{\circ}\mathrm{C}$ during the time τ_{Tmax} (in min) and at the pressure p (in 10^{-6} mbar), which both yield the dosage D_{Tmax} (in L). The total time and dosage, during which the sample is exposed to O_2 / H_2 (annealing and cooling), is given by τ_{tot} and D_{tot}, respectively. In an oxidation/reduction step, the O_2 / H_2 supply is stopped after the cooling of the sample down to 300 °C, despite for twoe reduction steps (no values for τ_{tot} and D_{tot}) where the H_2 supply is stopped after the annealing at $T_{\max}$.

No.	Step	p	τ_{Tmax}	τ_{tot}	D_{Tmax}	D_{tot}	Figure
0	10 min Ce deposition at RT						
1	Ox	3	10	35	1350	4730	Fig. 2(a) Fig. 3(a)
	Red	10^{-3}	30	85	UHV	UHV	Fig. S2
	Red	1	30	60	1350	2700	Fig. 2(b) Fig. 3(b) Fig. 4(a)
2	Ox	1	30	49	1350	2205	Fig. S3 Fig. 3(d) Fig. 4(c)
	Red	1	30	/	1350	/	Fig. S4(a)-(d) Fig. S5(a)
	Red	10	30	/	13500	/	Fig. S4(e),(f) Fig. S5(b)
3	Ox	1	30	48	1350	2160	Fig. 2(c) Fig. 3(e) Fig. 4(d)
	Red	20	60	79	54013	71117	Fig. 2(d),(e) Fig. 3(c) Fig. 4(b), Fig. S6
0	Clean Cu(111)						
/	Ox	1	5	22	225	990	Fig. 3(f),(g) Fig. 4(e) Fig. 5 Fig. S7(c)-(e)

surface. An image of this voltage is simultaneously obtained with the topography nc-AFM image and called *the CPD image*.

3. Results

3.1. KPFM experiments

After the preparation of a clean Cu(111) substrate, a typical surface morphology with wide atomically flat terraces and ML high steps as well as a typical LEED pattern are obtained (see figure 1(a) and (b)). On such a substrate, the ceria nanoparticles (NPs)

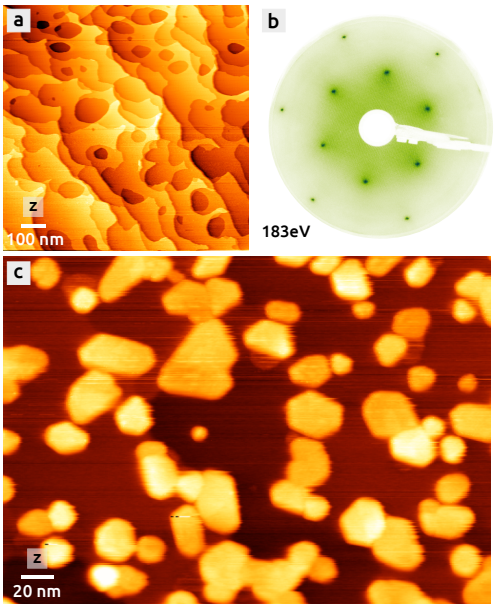

Figure 1. A typical large-scale STM topography image (a) and LEED pattern obtained at 183 eV (b), after the preparation of a clean Cu(111) surface. (c) A nc-AFM topography image of the same surface after the growth of ceria NPs. STM: $I = 0.18$ nA, $U_{Bias} = +2.32$ V, $v = 3.0$ Hz. nc-AFM: $\triangle f$ = -11.8 Hz, $f_0 = 74.0$, $v = 0.5$ Hz.

are grown and treated in several redox steps, which are all summarized in table 1.

The nc-AFM topography image in figure 1(c) shows the ceria NPs directly after the NP growth. Up to 40 nm large ceria NPs can be seen, covering about 40 % of the substrate. Owing to their 3D shape, the NPs exhibit various truncated shapes, with the NPs' edges forming mostly angles of 60° and 120°, which is due to their (111) epitaxy (see section 3.3). The mean NP height and density is around 4.2 nm and 1.0×10^{11} NPs/cm^2, respectively. Note that for all coverage and density values mentioned in this work, the error is around ± 8 % and $\pm 3 \times 10^{10}$ NPs/cm^2, respectively, because both parameters can change from surface site to surface site. Furthermore, due to the NP height distribution, the error of the mean height is around ± 0.5 nm.

A typical CPD image of the as-prepared ceria NPs is shown in figure 2(a). The image is composed of four horizontally aligned bands of alternating contrasts (1 to 4), which are parallel to the horizontal fast scanning direction. The contrast changes correspond to voltages changes in the range of 0.1 V. The abrupt changes of the contrast are due to changes of the tip's WF, which regularly appear during the imaging. As explained in detail in Ref. [55], the tip's WF can change upon re-arrangements of atoms or charges at the tip apex, which we believe is the reason here. When the tip's potential changes, the CPD between tip and surface changes in turn, producing bands as shown in the CPD image. Apart from the bands, a slight bright CPD contrast can be seen at the edges of the ceria NPs, which corresponds to a potential change of around +0.1 V with respect to the support and the top facets of the ceria NPs. With respect to the ceria NPs and the support, almost no contrast differences is visible;

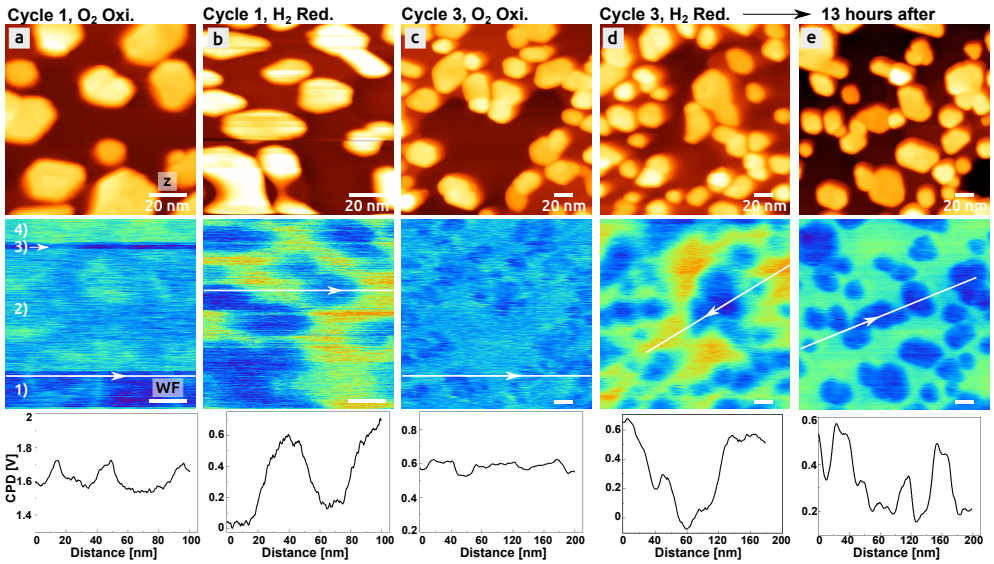

Figure 2. A selection of KPFM measurements obtained after successive redox steps listed in table 1. The top row of images are topography nc-AFM images whereas the images below are CPD images. For clarity, tip changes in the CPD image (c) are removed. Underneath each CPD image, a representative profile shows the potential at the respective white line in the CPD image above. All profiles have the same CPD range of 0.7 V. nc-AFM: $\triangle f$ = -13.7 (a), -4.5 (b), -22.0 (c), -17.0 (d) and -35.0 Hz (e), f_0 = 74.0 (a,b) and 76.5 kHz (c-e).

both regions seem to have more or less the same potential.

To check if the sample changes its morphology and/or surface potential upon UHV annealing only, the surface is annealed at 550 °C during 30 min (see figure S2 in the supplmentary information). Despite the long annealing at the quite elevated temperature, no changes can be detected in the NP morphology (NP height: 4.3 nm, NP coverage: 40 %, NP density: 1.2×10^{11} NPs/cm^2). The CPD image does not show any more the bright contrast at the edges of a NP but rather a decrease of the potential over the entire NP by -0.15 V with respect to the support.

In contrast to the UHV annealing, the surface potential changes considerably, when annealing the sample during the same time and at the same temperature in H_2 (1×10^{-6} mbar, 30 min, 1 350 L, 550 °C) as shown in figure 2(b): a clear dark contrast is visible at the ceria NPs, which corresponds to a potential decrease of up to -0.6 V with respect to the copper support. There is no enhanced bright contrast at the edges of the NPs and the surface morphology is almost the same as after the film preparation (NP height: 4.3 nm, NP coverage: 39 %, NP density: 0.8×10^{11} NPs/cm^2).

After this first O_2 / H_2 cycle, the sample is annealed in O_2 in cycle 2 with the same O_2 dosage from above (1×10^{-6} mbar, 30 min, 1 350 L, 550 °C). Similar phenomena as described for the as-prepared film can be observed (see figure S3(a) and (b) in the supplementary information): most importantly, the surface potential does not show any more the strong potential decrease at the NPs as in figure 2(b) but is rather homogeneous. Although a reduced potential can be seen at the ceria NPs after a following treatment in H_2 with same parameters used before (1×10^{-6} mbar, 30 min, 1 350 L, 550 °C) the potential difference is considerably smaller (-0.15 V) than above

(see figure S4(a) and (b) in the supplementary information). Even a higher H_2 dosage with a ten times higher dosage (1×10^{-5} mbar, 30 min, 13 500 L, 550 °C) shows a less strong potential difference of max. -0.4 V (see figure S4(e) and (f) in the supplementary information).

Starting with an oxidation step in cycle 3, same observations can be made as in the two oxidation steps before (figure 2(c)): in the CPD image, a faint enhanced bright contrast at the edges of the NPs and merely a slightly reduced potential of -0.1 V can be seen at the NPs. After a H_2 annealing at 550 °C, during which the sample is exposed to a very high H_2 dosage of 54 013 L (2×10^{-5} mbar, 60 min), a strong potential difference of -0.6 V can be observed at the ceria NPs, which yet again have the same morphology as before (NP height: 4.3 nm, NP coverage: 42 %, NP density: 1.0×10^{11} NPs/cm^2). Interestingly, by leaving the sample inside the UHV, the potential difference decreases by time such that after 13 hours, a maximum difference of only -0.4 eV can be observed (figure 2(e)) whereas after two days the difference decreases even onto -0.3 eV (see figure S6 in the supplementary information).

3.2. STM experiments

In the following, STM experiments are presented to comment the oxidation state of the Cu(111) support. Figure 3(a)-(e) present several atomically resolved STM images obtained after some of the redox steps listed in table 1.

Figure 3(a) shows the copper support directly after the Ce deposition and the following O_2 annealing in cycle 1: the surface is reconstructed and is composed of atomic features forming an ordered lattice with vertically oriented atomic rows. The unit cell represented by the red parallelogram has side lengths of $a = (8.2 \pm 0.5)$ Å and $b = (26.5 \pm 0.5)$ Å, and an angle of $\alpha = (89 \pm 1)°$ formed by a and b. Because of the O_2 annealing, a surface oxide has been created, which will be referred to as 'the new oxide structure' in the following (see Discussion Section). After the H_2 annealing in cycle 1, a typical atomic contrast of a small hexagonal lattice can be seen (figure 3(b)), which dimension equals indeed the one of the Cu(111) lattice. The same clean Cu(111) surface is obtained after the H_2 annealing in cycle 3 (figure 3(c)). Overall, the oxidized copper surface gets entirely reduced by H_2 to metallic Cu(111) in those two cases.

In cycle 2, the oxidized surface shows again a reconstructed Cu(111) surface with a unit cell that is comparable to the one of the new oxide structure (see figure S3c,d in the supplementary information). However, occasionally we also observe a slightly different structure (figure 3(d)) with a unit cell that is different in size ($a = (10.1 \pm 0.5)$ Å, $b = (21.9 \pm 0.5)$ Å, $\alpha = (86 \pm 1\,°)$) compared to the new oxide structure. The size of this structure is comparable to the one of the "44" oxide structure previously observed by STM [56, 57, 58, 26, 59]. In cycle 3, the new oxide structure is obtained again after the oxidation (figure 3(e)), with a dimension of the unit cell being quite similar compared to the one of the new oxide structure ($a = (8.8 \pm 0.5)$ Å, $b = (26.2 \pm 0.5)$ Å, $\alpha = (86 \pm 1)°$).

In general, after an oxidation of the sample, atomic sized defects are present on the copper oxide, depending on the surface site that is chosen for the imaging (see figure S3(c) in the supplementary information). As shown in figure 3(e), a defect disturbs the course of the atomic rows, which get displaced parallel to the row direction. This creates locally a different structure as shown by the orange parallelogram, which has a much smaller dimension with $a = (8.8 \pm 0.5)$ Å, $b = (17.2 \pm 0.5)$ Å and $\alpha = (86 \pm 1)°$. The size of this local structure is comparable with

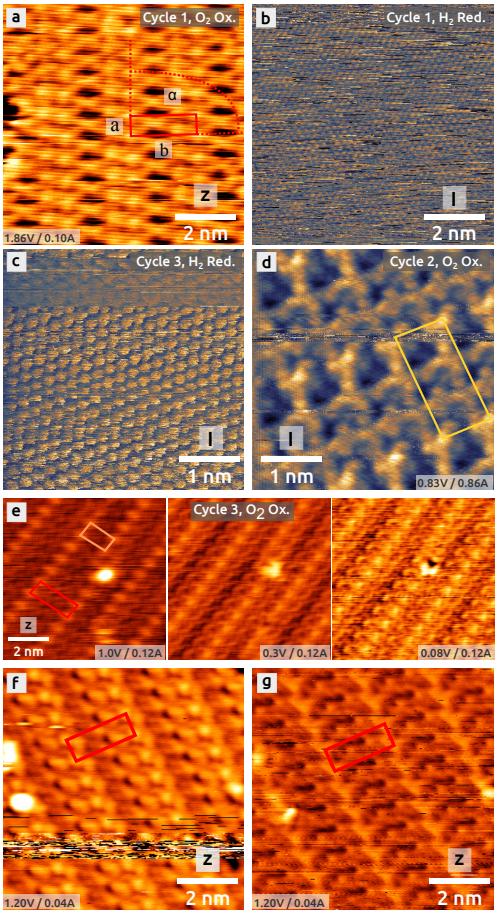

Figure 3. STM images obtained after a few selected redox steps listed in table 1 ((a)-(e)) and after an oxidation of only the Cu(111) surface without ceria ((f) and (g)). The images show the lattice of the copper oxide ((a), (d), (e)-(g)) and the clean metallic Cu(111) surface ((b) and (c)). Images ((a), (e)-(g)) and ((b)-(d)) are topography and current images, respectively. The images (f) and (g) show the same surface region (same scanning parameters). The red, yellow and orange parallelograms show three cells found on the oxidized Cu(111) surface. STM: $I = 0.10$ (a), 0.91 (b), 0.38 (c), 0.86 (d), 0.12 (e), 0.04 nA (f) and (g), $U_{Bias} = +1.86$ (a), $+0.37$ (b), $+0.47$ (c), $+0.83$ (d), $+1.0$,$+0.3$,$+0.08$ (e) and $+1.20$ V (f) and (g), $v = 5.0$ (a) and (b), 9.8 (c) and (e), 19.5 (d) and 6.5 Hz (f) and (g).

the one of the "29" oxide structure previously observed by STM [56, 57, 60, 26, 61, 59]. In some rare cases, we also observe a high defect density and in turn a quite irregular atomic structure as shown in figure S3(d) of the supplementary information and similar to previous observations on oxidized Cu(111) [57].

To compare the atomic contrast observed on the oxidized ceria/Cu(111) sample with the one of only the oxidized Cu(111) surface without ceria, a clean Cu(111) surface is prepared and oxidized at the same partial O_2 pressure and temperature of 550 °C (1×10^{-6} mbar, 5 min, 225 L at T_{max}). Two images obtained with same scanning parameters and at the same surface site are shown in figure 3(f) and (g). They differ in their atomic contrast due to a tip change that appears in another image

obtained between those two images (see figure S7d in the supplementary information). Independent on the contrast, the same dimension of the unit cell is observed with the side lengths $a = (9.3 \pm 0.5)$ Å, $b = (25.8 \pm 0.5)$ Å and an angle $\alpha = (87 \pm 1)°$. This structure, which we regularly observe on the oxidized Cu(111) surface, can be therefore assigned to the new oxide structure. Note that at the much lower oxidation temperature of 415 °C, we mostly observe the "29" oxide structure (figure S7(b) in the supplementary information).

Another regular observation is that the atomic contrast of the oxidized Cu(111) surface considerably changes when changing the bias voltage, e.g., from 1.0 to 0.08 V, as shown by the three images in figure 3(e). A similar voltage dependence was also observed before when imaging the "29" and "44" oxide structure [61, 59]. Because of this and because we also regularly observe the above mentioned contrast changes upon tip changes, we do not compare the relative atomic contrast of the images. For this, a comparison with theory is needed to localize the atomic positions inside the unit cell as done before [61, 59].

3.3. LEED experiments

Selected LEED experiments are shown in figure 4, which supply information averaged over a large surface region about the atomic lattice of the ceria NPs and the copper substrate. LEED images obtained at 27 (left column) and 60 eV (right column) show most important details.

After the reduction of the sample in cycle 1 and 3 (figure 4(a) and (b)), the LEED patterns show the typical diffraction spots for ceria (blue circles) and Cu(111) (red circles). Even if the contrast of the images is much enhanced, no other spots can be seen in between, also not at other electron energies in the range between 25 and 60 eV. The hexagonally arranged spots of ceria and Cu(111) is in agreement with the expected (111) orientation of CeO_x(111) and the Cu(111) support. The ratio of the reciprocal lattice vectors is around $r_{\mathrm{Red}} = 1.49 \pm 0.01$.

When oxidizing the sample, the typical diffraction spots for ceria (blue circles) and Cu(111) (red circles) can be found again, as exemplified with the sample oxidized in cycle 2 and 3 (figure 4(c) and (d)). The ratio of the reciprocal lattice vectors is a bit larger than before ($r_{\mathrm{Ox}} = 1.51 \pm 0.02$). A striking observation is, that there are many other, less bright LEED spots in between the ones originating from ceria and Cu(111). They can be best observed at relatively low electron energies between 15 and 30 eV, with 27 eV yielding the the best contrast. Note that the same spots can still be seen after the reduction experiments in cycle 2 (see figure S5 in the supplementary information), where the potential difference between ceria and the support is relatively small (see KPFM experiments above).

To understand if the latter diffractions spots originate from ceria or Cu(111), a clean Cu(111) surface without ceria is oxidized under the same oxidation conditions (1×10^{-6} mbar, 5 min, 225 L, 550 °C). The resulting LEED images are shown in figure 4(e): at 60 eV, the typical hexagonally arranged Cu(111) spots are present. All the other spots of smaller intensity, which can be seen in particular at 27 eV, coincide almost perfectly with the additional spots of the oxidized ceria/Cu(111) sample (see, e.g., yellow ellipse). Figure 5 shows the LEED spots at 51 eV in a high contrast: two types of rows can be seen (arrows), which corresponds to the atom rows visible in the STM images and which are rotated by 30° to each other due to two domains that are present on the surface. At some places, we can estimate the location of the unit cell

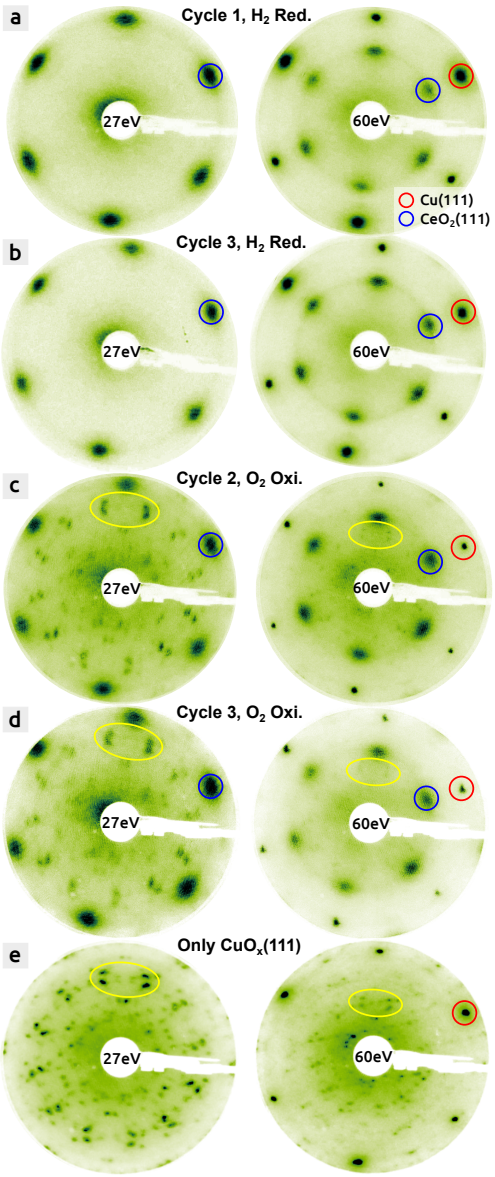

Figure 4. (a)-(d) LEED images obtained at 27 (left) and 60 eV (right) on the ceria/Cu(111) sample, after a few selected redox steps listed in table 1. (e) The LEED patterns of an oxidized Cu(111) surface without ceria. The blue and red circles show the typical diffraction spots for ceria and Cu(111), respectively, whereas the yellow ellipses are a guide to the eye to mark a few spots of the copper oxide that can be seen at 27 and 60 eV.

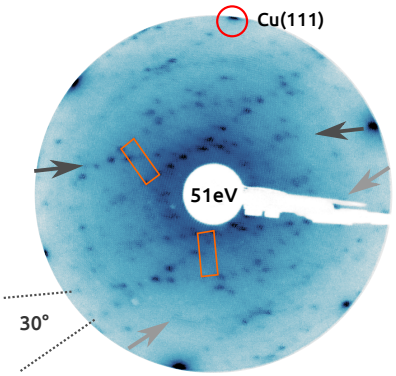

Figure 5. The LEED pattern of an oxidized Cu(111) surface without ceria obtained at 51 eV. The orange parallelograms mark the unit cell, which matches the one of the new oxide structure.

(orange parallelogram), which matches the one of the new oxide structure. Overall, we can assign the additional spots in figure 4(c) and (d) to the copper oxide rather than to the supported ceria.

4. Discussion

In the following, we discuss the oxidation and reduction of the ceria/Cu(111) catalyst separately with help of figure 6, which sketches the oxidation/reduction state of the sample in dependence on the eight redox steps.

4.1. Oxidation

The oxidation of the Cu(111) surface was extensively studied by LEED [62, 57], μLEED/LEEM [63], XPS [64] and STM [56, 57, 60, 58, 61, 65, 64, 59], in particular in dependence on the temperature of the O_2 annealing (from RT to 450°C) and post-annealing [60, 57]. The overall conclusion is that the surface reconstructs at temperatures starting at ∼300 °C, forming the "29" and "44" oxide structures [56]. It is therefore not astonishing that during an O_2 annealing step at 550 °C (figure 6(a), (d) and (g)) the Cu(111) surface also oxidises in the presence of ceria islands or NPs that only partially cover the copper substrate, as indeed observed before [26, 35] and shown in this work.

However, in contrast to the latter work, we observe an oxide structure, which is much larger than the "29" oxide structure ($a_{29} = 9.2$ Å, $b_{29} = 17.9$ Å) and which is different to the "44" oxide structure ($a_{44} = 11.7$ Å, $b_{44} = 21.9$ Å) [56]. Our LEED data supports this new oxide structure: i) the diffraction spots do not match the spots of previously published LEED data of the "29" and "44" oxide structure [62, 57, 63]. ii) As shown in figure 5, we can find the unit cell of the new oxide structure in its correct shape. Note that the unit cell is clearly different compared to the unit cells of the "29" and "44" oxide structure found by μLEED [63].

A previously published work [26] reports on a new oxide structure, which is formed by supported ceria islands: the ceria islands enhance the dissociation of O_2 and the oxide propagates from the islands. Unfortunately, no dimensional parameters of the

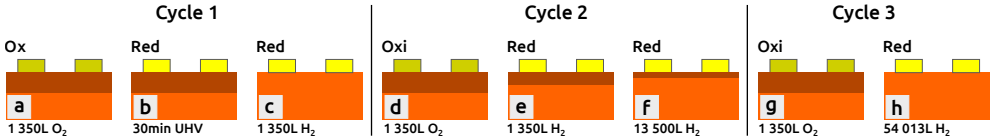

Figure 6. Sketches of the ceria/Cu(111) oxidation state after all the eight redox steps conducted within 3 cycles at 550 °C (see table 1). The O_2 and H_2 dosage is mentioned at the bottom of the figure for each step. The copper support in its metallic state is drawn in an orange color whereas the surface oxide has a dark orange contrast, with the thickness illustrating the oxidation depth of the Cu(111) surface. Completely oxidized ceria is drawn in dark yellow whereas ceria is in yellow after a reduction step.

unit cell are mentioned in this work although the shape of the unit cell seems to be similar to the one which we regularly observe (compare with figure 3b in Ref. [26]). Note that the annealing temperature used in the latter work (5×10^{-7} torr, 20 min, 600 L, 427 °C) is much lower compared to our temperature (1×10^{-6} mbar, 30 min, 1 350 L, 550 °C). If our new oxide structure is the same as the one in Ref. [26], we anticipate that our $\triangle T = 123$ °C higher temperature is the reason for the different observations made in Ref. [26] and here: we speculate that when oxidizing the system at 427 °C, not enough thermal energy is present for the new oxide creation and that ceria is needed to help in the way described in Ref. [26]. However, enough thermal energy is present at 550 °C where ceria is not necessarily needed. In particular calculations have to reveal in future the detailed mechanisms involved in the oxide formation.

Comparing the values of the unit cell dimension, which we obtain from several atomically resolved STM images, the values deviate a bit from each other. The reason is that our STM/AFM works at RT where in particular the drift of the x, y, z scanner deforms the lattice. The drift varies from time to time so that slightly different values for the unit cell are obtained. Considering the values from above, we assume that the unit cell has a dimension given by $a = (9 \pm 1)$ Å, $b = (26 \pm 1)$ Å and $\alpha = (88 \pm 2)°$. In comparison to the "44" structure ($a_{44} = 11.7$ Å, $b_{44} = 21.9$ Å), our new structure is thinner and longer. To find the exact positions of all atoms inside the unit cell, a comparison between STM and density function theory (DFT) like in Refs. [58, 61, 59] has to be done in future.

With respect to the ceria, we could not obtain the atomic resolution on the NP top facets, which is probably due to the high bias voltage that has to be used for a stable imaging ($U_{\mathrm{Bias}} > 3$ V). The only information about the atomic lattice comes from LEED, which shows that the ceria NPs grow in their preferred (111) epitaxy. LEED supplies a value of $r_{\mathrm{Ox}} = 1.51 \pm 0.02$ for the ratio of the reciprocal lattice vectors between ceria and Cu(111), being comparable with the previously found value of 1.5 [28, 31, 32]. With the lattice constant of $a_{\mathrm{Cu,lit,exp}} = (3.61 \pm 0.01)$ Å for Cu (see table S1 in the supplementary information), we obtain a lattice constant of $a_{\mathrm{CeO2,exp}} = (5.45 \pm 0.09)$ Å, which is in good agreement with the experimental value of $a_{\mathrm{CeO2,lit,exp}} = (5.41 \pm 0.01)$ Å obtained by X-ray scattering (see table S2 in the supplementary information). Overall, the nanometre thick ceria NPs in their fully oxidized state are not strained by the support and form an ordered oxide. The lattice of the oxide is commensurate and aligned with the principal crystallographic axes of the substrate as observed before for thinner ceria islands [31].

With respect to the ceria oxidation state, we can assume that the ceria NPs are made from stoichiometric CeO_2, as this was previously measured by XPS on similar thick ceria films (5-6 ML: [31, 33], 12 ML: [30]). In the latter work, samples were oxidized under similar oxidation conditions. Note that any possible contamination like OH or carbon species are removed by the oxygen annealing [66, 23], so that the ceria surface is also free from contamination.

It is surprising that no strong CPD difference between the ceria NPs and Cu(111) can be seen, after an oxidation step is done. In some cases, we observe no difference at all, in other cases we observe a slight reduction of -0.1 V above the ceria NPs. The reason for this remains unknown so far. The bright contrast at the edges of the ceria NPs can be assigned to a more negative potential at the edges, probably produced by low coordinated negative atomic species like unscreened O ions as observed before on thick ceria films [67] and similar ionic surfaces like $CaF_2(111)$ [68].

4.2. Reduction

After a sufficiently strong H_2 reduction in the kilo Langmuir range at 550°C, the copper substrate gets entirely reduced to metallic Cu(111) in cycle 1 and 3 (figure 6(c) and (h)), as it is evident from our STM and LEED data. The H_2 dosage may vary at 550 °C: as observed in cycle 3, a high dosage of 54 000 L is needed to entirely reduce the copper oxide whereas the dosage in cycle 1 is only 1 350 L high. The latter could not be reproduced in cycle 2, after which a H_2 anneal with 1 350 L and even 13 500 L of H_2 (figure 6(e) and (f)) leads to a potential difference of only -0.4 V and to a LEED pattern with the additional spots of the oxide still included.

Table 1 shows that the oxidation time is 10 minutes long in cycle 1 whereas the one in cycle 2 is 30 minutes long, however, with a three times smaller O_2 pressure compared to cycle 1. We speculate that due to the longer oxidation time in cycle 2, deeper subsurface layers of the copper support get oxidized than in cycle 1. As a consequence, the H_2 dosage has to be higher in cycle 2 than in cycle 1, as indeed shown by cycle 3 (exact same oxidation conditions as in cycle 2). This means that only a part of the oxide could be reduced upon the two H_2 dosages in cycle 2 (figure 6(e) and (f)). Note that the O_2 partial pressure values and related dosage values used in the work here are more elevated with respect to the 'standard pressure' of 5×10^{-5} mbar used in literature so that an oxidation of sub-surface regions is reasonable in our case.

Overall, H_2 can be used as an reducing agent for an oxidized Cu(111) surface similar to CO [21, 26]. Our work shows that due to the high temperature of 550 °C the reduction is much faster compared to a H_2 reduction at RT, at which a very high pressure of 1.5 torr during 26 hours is obviously needed [19].

With respect to the ceria NPs, we observe the perfect LEED pattern of the ceria (111) epitaxy and the metallic Cu(111) surface after a complete H_2 reduction. The slightly smaller value for the ratio of the reciprocal lattice vectors between ceria and Cu(111) ($r_{\mathrm{Red}} = 1.49 \pm 0.01$) yields a slightly smaller lattice constant of (5.38 ± 0.05) Å compared to the experimental value of $a_{\mathrm{CeO2,lit,exp}} = (5.41 \pm 0.01)$ Å (see table S2 in the supplementary information). This ∼0.6 % small lattice contraction points to a possible lattice strain that is build up during the reduction, which has to be studied in more detail by future experiments.

There are no additional spots that appear in the LEED images in the energy range between 25 and 60 eV. This is quite surprising in view of the high temperature of 550 °C and the high H_2 dosage as well as in view of previous LEED observations

[33, 34, 37]: the latter show that upon reduction by additional deposited Ce on 2-3 ML high ceria islands, which cover 50 % of the Cu(111) surface, the atomic structure changes due to a loss of oxygen and the related reduction of Ce^{4+} to Ce^{3+} [37]. This considerably changes the LEED pattern starting with the ι-Ce_7O_{12} R19° phase ($CeO_{1.71}$) and ending with the entirely reduced Ce_2O_3 phase ($CeO_{1.5}$). The same ι-Ce_7O_{12} R19° phase is also the first phase that appears on 250 nm thick ceria films upon reduction [69]. All the latter LEED data let assume that the reduction of the ceria NPs in our work cannot be so high, eventually well below 50 %. Indeed, XPS shows that the efficiency of the H_2 reduction is quite low: when annealing the sample at 427 °C in 1.5×10^{-6} mbar H_2, about 20 hours are needed to obtain a 24 % large reduction [41]. A very recent micro X-Ray absorption spectroscopy (μXAS-PEEM) study shows that the degree of reduction remains low ($CeO_{\sim 1.9}$) if a stoichiometric CeO_2(111) film is reduced by annealing at 550 °C during a dosage of 26 000 L of H_2 [70]. We therefore anticipate, that the degree of reduction is less than 20 %.

When the copper oxide is entirely reduced, we measure a potential difference of up to -0.6 V between the ceria NPs and Cu(111). Because the contact potential difference (CPD) between the sample and tip is determined by the WFs of both, $CPD = (\phi_{sample} - \phi_{tip}) / e$), the potential difference between Cu(111) and ceria on Cu(111) is related to the WF difference at these surface sites: $CPD_{rCeria/Cu} - CPD_{Cu} = (\phi_{rCeria/Cu} - \phi_{Cu}) / e = \triangle\phi_{rCeria/Cu\text{-}Cu} / e$. Note that WF differences measured by KPFM can deviate from the true value due to the long-range electrostatic tip-surface interaction and the related tip-surface convolution effect: in the case of a blunt tip, the CPD includes also contributions from the Cu(111) surface if the tip is placed directly above a ceria NP. As a result, the contrast is blurred at the edges and a smaller value for $\triangle\phi$ is measured. Although the CPD well saturates in the middle of the up to 40 nm large ceria NPs (see figure 2(b), (d) and (e)) we nevertheless assume that the measured WF difference describes a lower limit.

With the WF difference of $\triangle\phi_{rCeria/Cu\text{-}Cu} \approx$ -0.6 eV between the ceria NPs and the clean Cu(111) surface (see figure 7 (a)), and with the absolute WF of $\phi_{Cu(111)} = (4.90 \pm 0.02)$ eV for Cu(111), the absolute WF of ceria/Cu(111) is around $\phi_{rCeria/Cu} \approx 4.3$ eV. Interestingly, the same WF reduction of $\triangle\phi_{rCeria/Pt\text{-}Pt} \approx$ -0.6 eV could be observed after reduction of ceria films on the Pt(111) surface [23], which has a considerably high WF ($\phi_{Pt(111)} = (5.90 \pm 0.02)$ eV), lifting therefore the WF of ceria onto $\phi_{rCeria/Pt} \approx 5.3$ eV. This comparison clearly shows that KPFM is not measuring the WF of the ceria NPs alone but rather the WF of the metal underneath, under the influence of the ceria film. Interestingly, the WF difference decreases on a time scale of days when the sample is left in the UHV. As KPFM has shown to be very sensitive on adsorbed species on surfaces [71], we strongly anticipate that the sample gets contaminated by species from the residual gas of the UHV. Such contamination was observed also on PdNPs [72] and we suspect that it is in particular the reactive Cu(111) surface that reacts with the residual gas.

A very important difference with respect to the ceria/Pt(111) case is that the CPD contrast of the support is always homogeneous and constant, in particular after a complete H_2 reduction. Therefore, we can assume that there is no local alloying effect between Cu and Ce such that destinctive regions of pure Cu(111) and regions of the alloy are created as in the case of ceria/Pt(111) [23]. A strong support comes from the morphology of the ceria NPs, where neither the coverage nor the height of the NPs noticeable changes upon a redox step unlike on ceria/Pt(111) [23]. In other words, no large amount of Ce is liberated during the reduction to form an alloy with

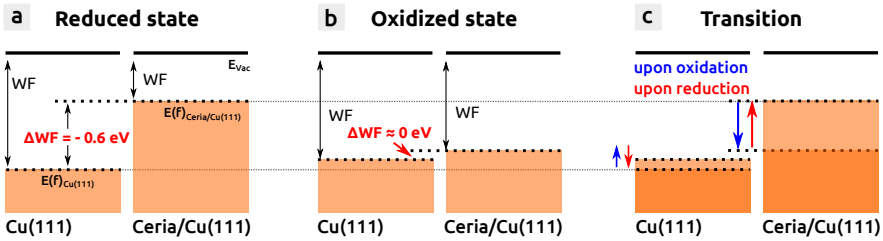

Figure 7. The WF state of ceria/Cu(111) and Cu(111) in the energy level diagram after reduction (a) and oxidation (b). Image (c) shows a possible trend of the WF change during oxidation and reduction. The Fermi and vacuum levels are denoted by E(f) and E_{Vac}.

Cu. Note that we also always observe the perfect LEED spots of ceria and Cu(111) but no other spots and that we always observe the perfect Cu(111) lattice in STM.

In comparison, the fully oxidized ceria/Cu(111) system has a WF difference close to zero ($\triangle\phi_{\text{Ceria/Cu-Cu}} \approx$ -0.1 . . . 0 eV) (figure 7(b)). The question is, if one of the sites or both change their WF upon oxidation or reduction. A DFT calculation shows that the WF of stoichiometric $Cu_2O(111)$ is almost the same as the one of Cu(111) [73] (5.09 eV for Cu(111) versus 5.03 eV for $Cu_2O(111)$). This means that upon reduction it is the ceria NPs on Cu(111), which decrease their WF by -0.6 eV (figure 7(c)). Partial support comes from the unsuccessful H_2 reduction experiments in cycle 2 (see figure S4 in the supplementary information): the copper oxide is still present but the WF difference between the ceria NPs and the copper support has decreased by -0.4 eV, pointing to a contribution of only the Ceria/Cu(111) WF. We speculate that when the copper support gets finally reduced by a following H_2 reduction such as in cycle 3, the WF difference decreases furthermore onto -0.6 eV because the copper support is then in its metallic Cu(111) state slightly increasing its WF (figure 7(c)). At this point, we clearly stress that our hypothesis has to be further investigated in future. We believe that in particular calculations such as in Ref. [59] have to be accomplished with respect to the WF of the new oxide structure because our new oxide structure differs considerably with respect to the one used in Ref. [73].

5. Conclusion

With help of our results obtained by LEED, STM, nc-AFM and KPFM, we comment on the redox behaviour of the inverse catalyst ceria/Cu(111). With the temperature increasing from RT to 550 °C and due to the relative high O_2 partial pressure of 10^{-6} mbar, up to 4 nm high ceria NPs are created on Cu(111), which cover about 40 % of the copper surface. The oxidation state of this system can be changed at will from a fully oxidized to a partially reduced state:

Upon oxidation with O_2 and with the sample at 550 °C, the ceria NPs and Cu(111) support get both oxidized as shown by STM with atomic resolution. We find a new copper oxide structure with a unit cell ($a = (9\pm1)$ Å, $b = (26\pm1)$ Å, $\alpha = (88 \pm 2)°$), which is thinner and longer than the known "44" oxide structure. We observe the same structure also on only Cu(111) without ceria and assume that it is in particular the high temperature of 550 °C, which is responsible for the creation of this new oxide structure.

An entire reduction of the oxidized copper substrate with H_2 in the 10^{-6} mbar range requires a high temperature of 550 °C and high H_2 dosage values in the range between 1 and some 10s of kL, depending on the thickness of the previously created copper oxide. Afterwards, the hexagonal lattice of the Cu(111) surface can be seen by STM. Because no LEED spots can be observed that can be assigned to a possible strong reduction of the ceria NPs we estimate that a reduction of the ceria NP is below 20 %.

After a complete H_2 reduction, we measure a lower limit of $\triangle\phi_{\mathrm{rCeria/Cu\text{-}Cu}} \approx$ -0.6 eV for the WF difference between ceria NPs and the clean Cu(111) surface. In comparison with our recent work on ceria/Pt(111) [23], our measurements clearly exemplify that KPFM is measuring the WF of ceria on Cu(111) and not ceria alone. After a complete oxidation of the surface, the WF difference is close to zero ($\triangle\phi_{\mathrm{Ceria/Cu\text{-}Cu}} \approx$ -0.1 . . . 0 eV). We speculate that upon oxidation it is ceria, which increases its WF, but also the copper oxide, which slightly decreases its WF. Thanks to KPFM we can assume that there is no strong alloying effect between Cu and Ce during the reduction unlike the case ceria/Pt(111) [23]: the surface potential is homogeneous and constant on the copper support, only the (111) lattice of Cu is observed by STM and the ceria NP morphology (NP size and height) does not change upon a redox step unlike on ceria/Pt(111) [23].

Acknowledgements

Support from the *Agence Nationale de la Recherche* (ANR) through project *REACTIVITY* (grant ANR-17-CE09-0045) and *CHAMAN* (grant ANR-17-CE24-0011) is gratefully acknowledged. We thank J Falta, J-I Flege, L. Pleines, L Glatthaar, M Reichling and A Soon for stimulating discussions.

ORCID iDs

A El Barraj https://orcid.org/0000-0002-9947-6935
B Chatelain https://orcid.org/0000-0003-3121-0409
C Barth https://orcid.org/0000-0003-4250-4533

References

[1] Montini T, Melchionna M, Monai M and Fornasiero P 2016 *Chem. Rev.* **116** 5987–6041
[2] Devaiah D, Reddy L H, Park S E and Reddy B M 2018 *Catal. Rev.* **60** 177–277
[3] Paier J, Penschke C and Sauer J 2013 *Chem. Rev.* **113** 3949–85
[4] Ratnasamy C and Wagner J P 2009 *Catal. Rev.* **51** 325–440
[5] Gorte R J 2010 *AIChE J.* **56** 1126–1135
[6] Fan L, Wang C, Chen M and Zhu B 2013 *J. Power Sources* **234** 154–174
[7] Shaikh S P S, Muchtar A and Somalu M R 2015 *Renew. Sustain. Energy Rev.* **51** 1–8
[8] Fiala R, Figueroba A, Bruix A, Vaclavu M, Rednyk A, Khalakhan I, Vorokhta M, Lavkova J, Illas F, Potin V, Matolinova I, Neyman K M and Matolin V 2016 *Appl. Catal. B Environ.* **197** 262–270
[9] Matsumoto S 2004 *Catal. Today* **90** 183–190
[10] Niu G, Zoellner M H, Schroeder T, Schaefer A, Jhang J H, Zielasek V, Bäumer M, Wilkens H, Wollschläger J, Olbrich R, Lammers C and Reichling M 2015 *Phys. Chem. Chem. Phys.* **17** 24513–24540
[11] Freund H J 2010 *Chem. Eur. J.* 9384 – 9397
[12] Luches P and Valeri S 2015 *Materials* **8** 5818–5833
[13] Mullins D R 2015 *Surf. Sci. Rep.* **70** 42–85

[14] Rodriguez J A, Grinter D C, Liu Z, Palomino R M and Senanayake S D 2017 *Chem. Soc. Rev.* **46** 1824–1841
[15] Beran J and Mašek K 2019 *Vacuum* **167** 438–444
[16] Wilson E L, Grau-Crespo R, Pang C L, Cabailh G, Chen Q, Purton J A, Catlow C R A, Brown W A, de Leeuw N H and Thornton G 2008 *J. Phys. Chem. C* **112** 10918–10922
[17] Lu J L, Gao H J, Shaikhutdinov S and Freund H J 2007 *Catal. Letters* **114** 8–16
[18] Luches P, Pagliuca F, Valeri S, Illas F, Preda G and Pacchioni G 2012 *J. Phys. Chem. C* **116** 1122–1132
[19] Graciani J, Mudiyanselage K, Xu F, Baber A E, Evans J, Senanayake S D, Stacchiola D J, Liu P, Hrbek J, Sanz J F and Rodriguez J A 2014 *Science* **345** 546–550
[20] Senanayake S D, Ramírez P J, Waluyo I, Kundu S, Mudiyanselage K, Liu Z, Liu Z, Axnanda S, Stacchiola D J, Evans J and Rodriguez J A 2016 *J. Phys. Chem. C* **120** 1778–1784
[21] Rodriguez J A, Graciani J, Evans J, Park J B, Yang F, Stacchiola D, Senanayake S D, Ma S, Pérez M, Liu P, Sanz J F and Hrbek J 2009 *Angew. Chemie Int. Ed.* **48** 8047–8050
[22] Schierbaum K D 1998 *Surf. Sci.* **399** 29–38
[23] Gasperi G, Luches P and Barth C 2018 *J. Phys. Chem. C* **122** 25954–25963
[24] Zhao X, Ma S, Hrbek J and Rodriguez J A 2007 *Surf. Sci.* **601** 2445–2452
[25] Hasegawa T, Shahed S M F, Sainoo Y, Beniya A, Isomura N, Watanabe Y and Komeda T 2014 *J. Chem. Phys.* **140** 044711
[26] Yang F, Graciani J, Evans J, Liu P, Hrbek J, Sanz J F and Rodriguez J A 2011 *J. Am. Chem. Soc.* **133** 3444–3451
[27] Mysliveček J, Matolín V and Matolínová I 2015 *Materials* **8** 6346–6359
[28] Siokou A and Nix R M 1999 *J. Phys. Chem. B* **103** 6984–6997
[29] Siokou A and Nix R M 1999 *J. Phys. Chem. B* **103** 6984–6997
[30] Wrobel R, Suchorski Y, Becker S and Weiss H 2008 *Surf. Sci.* **602** 436–442
[31] Šutara F, Cabala M, Sedláček L, Skála T, Škoda M, Matolín V, Prince K C and Cháb V 2008 *Thin Solid Films* **516** 6120–6124
[32] Staudt T, Lykhach Y, Hammer L, Schneider M A, Matolín V and Libuda J 2009 *Surf. Sci.* **603** 3382–3388
[33] Stetsovych V, Pagliuca F, Dvořák F, Duchoň T, Vorokhta M, Aulická M, Lachnitt J, Schernich S, Matolínová I, Veltruská K, Skála T, Mazur D, Mysliveček J, Libuda J and Matolín V 2013 *The Journal of Physical Chemistry Letters* **4** 866–871
[34] Duchon T, Dvořák F, Aulická M, Stetsovych V, Vorokhta M, Mazur D, Veltruská K, Skala T, Myslivecek J, Matolínová I and Matolin V 2013 *J. Phys. Chem. C* **118** 357–365
[35] Hu S, Wang Y, Wang W, Han Y, Fan Q, Feng X, Xu Q and Zhu J 2015 *J. Phys. Chem. C* **119** 3579–3588
[36] Wang Y, Hu S, Xu Q, Ju H and Zhu J 2018 *Top. Catal.* **61** 1227–1236
[37] Tovt A, Stetsovych V, Dvorák F, Johánek V and Mysliveček J 2019 *Appl. Surf. Sci.* **465** 557–563
[38] Mašek K, Beran J and Matolín V 2012 *Appl. Surf. Sci.* **259** 34–38
[39] Höcker J, Duchon T, Veltruská K, Matolín V, Falta J, Senanayake S D and Flege J I 2016 *J. Phys. Chem. C* **120** 4895–4901
[40] Duchoň T, Hackl J, Höcker J, Veltruská K, Matolín V, Falta J, Cramm S, Nemšák S, Schneider C M, Flege J I and Senanayake S D 2017 *Ultramicroscopy* **183** 84–88
[41] Duchon T, Hackl J, Mueller D N, Kullgren J, Du D, Senanayake S D, Mouls C, Gottlob D M, Khan M I, Cramm S, Veltruská K, Matolín V, Nemšák S and Schneider C M 2020 *J. Mater. Chem. A* **8** 5501–5507
[42] Škoda M, Cabala M, Matolínová I, Skála T, Veltruská K and Matolín V 2010 *Vacuum* **84** 8–12
[43] Happel M, Lykhach Y, Tsud N, Skála T, Prince K C, Matolín V and Libuda J 2011 *J. Phys. Chem. C* **115** 19872–19882
[44] Chen B, Ma Y, Ding L, Xu L, Wu Z, Yuan Q and Huang W 2013 *J. Phys. Chem. C* **117** 5800–5810
[45] Hu S, Wang W, Wang Y, Xu Q and Zhu J 2015 *J. Phys. Chem. C* **119** 18257–18266
[46] Wang W J, Wang Y, Xu Q, Ju H X, Wang T, Tao Z J, Hu S W and Zhu J F 2017 *Chinese Chem. Lett.* **28** 1760–1766
[47] Wang Y, Li X, Hu S, Xu Q, Ju H and Zhu J 2018 *Acta Physico-Chimica Sin.* **34** 1381–1389
[48] Lykhach Y, Skála T, Neitzel A, Tsud N, Beranová K, Prince K C, Matolín V and Libuda J 2020 *Chinese J. Catal.* **41** 985–997
[49] Szabová L, Stetsovych O, Dvořák F, Farnesi Camellone M, Fabris S, Mysliveček J and Matolín V 2012 *J. Phys. Chem. C* **116** 6677–6684
[50] Graciani J, Vidal A B, Rodriguez J A and Sanz J F 2014 *J. Phys. Chem. C* **118** 26931–26938
[51] Yang B X, Luo Y and Ye L P 2018 *J. Mol. Model.* **24** 20

[52] Luches P, Pagliuca F and Valeri S 2014 *Phys. Chem. Chem. Phys.* **16** 18848–18857
[53] Barth C, Claeys C and Henry C R 2005 *Rev. Sci. Instr.* **76** 083907
[54] Kitamura S, Suzuki K and Iwatsuki M 1999 *Appl. Surf. Sci.* **140** 265–270
[55] Barth C, Hynninen T, Bieletzki M, Henry C R, Foster A S, Esch F and Heiz U 2010 *New J. Phys.* **12** 093024
[56] Jensen F, Besenbacher F and Stensgaard I 1992 *Surf. Sci.* **269-270** 400–404
[57] Matsumoto T, Bennett R, Stone P, Yamada T, Domen K and Bowker M 2001 *Surf. Sci.* **471** 225–245
[58] Yang F, Choi Y, Liu P, Hrbek J and Rodriguez J A 2010 *J. Phys. Chem. C* **114** 17042–17050
[59] Lee Y J, Ly T T, Lee T, Palotás K, Jeong S Y, Kim J and Soon A 2021 *Appl. Surf. Sci.* **562** 150148
[60] Wiame F, Maurice V and Marcus P 2007 *Surf. Sci.* **601** 1193–1204
[61] Therrien A J, Zhang R, Lucci F R, Marcinkowski M D, Hensley A, McEwen J S and Sykes E C H 2016 *J. Phys. Chem. C* **120** 10879–10886
[62] Judd R W, Hollins P and Pritchard J 1986 *Surf. Sci.* **171** 643–653
[63] Höcker J, Cartas W, Schaefer A, Bäumer M, Weaver J F, Falta J and Flege J I 2015 *J. Phys. Chem. C* **119** 14175–14184
[64] Waluyo I, Mudiyanselage K, Xu F, An W, Liu P, Boscoboinik J A, Rodriguez J A and Stacchiola D J 2019 *J. Phys. Chem. C* **123** 8057–8066
[65] Matencio S, Barrena E and Ocal C 2016 *Phys. Chem. Chem. Phys.* **18** 33303–33309
[66] Barth C, Laffon C, Olbrich R, Ranguis A, Parent P and Reichling M 2016 *Sci. Rep.* **6** 21165
[67] Olbrich R, Pieper H H, Oelke R, Wilkens H, Wollschläger J, Zoellner M H, Schroeder T and Reichling M 2014 *Appl. Phys. Lett.* **104** 081910
[68] Pieper H H, Barth C and Reichling M 2012 *Appl. Phys. Lett.* **101** 051601
[69] Wilkens H, Schuckmann O, Oelke R, Gevers S, Reichling M, Schaefer A, Bäumer M, Zoellner M H, Niu G, Schroeder T and Wollschläger J 2013 *Phys. Chem. Chem. Phys.* **15** 18589–18599
[70] Pleines L, Buß L, Mentes T O, Genuzio F, Locatelli A, Falta J and Flege J I 2021 *For submission to: J. Phys: Condens. Matter.*
[71] Grönbeck H and Barth C 2019 *J. Phys. Chem. C* **123** 24615–24625
[72] Palacios-Lidon E, Henry C R and Barth C 2014 *ACS Catal.* **4** 1838–1844
[73] Chiter F, Costa D, Maurice V and Marcus P 2020 *J. Phys. Chem. C* **124** 17048–17057